Universitat de Barcelona
June 23, 2016

Can the Tremaine - Weinberg method be used to determine the pattern speed of the bar and the spiral arms of the Milky Way?

Master thesis

Marta Reina Campos[1,2,⋆]
Supervisor: Francesca Figueras[1]
Advisors: Teresa Antoja[2], Mercè Romero-Gómez[1] and Santi Roca-Fàbrega[3]

[1] Departament de Física Quàntica i Astrofísica, Institut de Ciències del Cosmos de la Universitat de Barcelona (IEEC-UB), Martí i Franquès, 1, 08028 Barcelona, Spain
e-mail: mreina@am.ub.es
[2] Directorate of Science, European Space Agency (ESA-ESTEC), PO Box 299, 2200 AG Noordwijk, The Netherlands
[3] Racah Institute of Physics, The Hebrew University of Jerusalem, Edmond J. Safra Campus, Givat Ram, Kaplun building, office 110, 91904 Jerusalem, Israel

ABSTRACT

Context. The pattern speed of the non-axisymmetric structures of the galactic disc is a key parameter to understand the dynamics in the Milky Way. For neither the Galactic bar nor the spiral arms it is well determined. All previous determinations have large uncertainties associated avoiding to shed some light on the nature of these structures.
Aims. To evaluate whether the Tremaine-Weinberg method, as derived by Debattista et al. (2002), for the determination of the pattern speed of the Galactic bar and the spiral arms is going to be applicable to the upcoming radial velocity data from large surveys like Gaia, APOGEE, WEAVE and 4MOST.
Methods. We start using simplistic test particles simulations of either Galactic bar or TWA spiral arms to see how the method behaves and we give a first insight on N-body simulations. We keep on using each time more realistic models until using Gaia mock catalogues. We characterize the capability of the method by doing a study for di-erent sample sizes, di-erent galactic tracers and by evaluating the statistical and systematic errors induced by the insterstellar extinction and the Gaia errors.
Results. The derivation of the angular speed of the spiral arms requires full galactic longitude coverage and the availability of stellar tracers up to at least $r \simeq 2-3$ kpc from the Sun, whereas for the Galactic bar, the data can be constrained to the inner disc but tracers have to reach $r \simeq 5-6$ kpc. We check that both hot and cold populations may be used as long as the size of the sample is of $N \sim 10^6$.
Conclusions. The Tremaine - Weinberg method applied to RVS Gaia data form Red Clump stars is potentially a good tool to derive the pattern speed of the spiral arms. Its application to the galactic bar shall wait for deeper spectroscopic surveys.

Key words. galaxy dynamics – Milky Way – pattern speed – spiral arms – Galactic bar – Tremaine-Weinberg method

Contents

⋆ Master student

1. Introduction

Despite the common idea that the structure of the Milky Way is fairly well understood, there are still many open questions about its origin and properties. In the case of the Galactic bar, there has been some debate in the recent years about the presence of a long bar, which would be tilted approximately 20º with respect to the COBE/DIRBE bar and it would be ∼ 1 kpc longer (López-Corredoira et al. 2007). On the other hand, the geometry of the spiral structure is still unknown, as different tracers give different estimates of the pitch angle and the number of arms (Vallée 2008, 2015).

The first suggestion of the Milky Way being a barred galaxy comes from Vaucouleurs (1964), as an explanation to the non-asymmetry observed in radio maps. The first evidence of a bar-like distribution in the stars of the inner Galaxy was observed in source counts [Weinberg 1992; Hammersley et al. 1994; Stanek et al. 1994] and in asymmetries in the infrared surface brightness maps [Blitz & Spergel 1991; Dwek et al. 1995] that systematically showed more stars at positive galactic longitudes ($l \leq 30^o$) near the Galactic Plane. Nowadays there is consensus on the presence of a stellar bar in the inner Galaxy, but the researchers are still discussing the exact nature of it. Cabrera-Lavers et al. (2007) evaluates the possibility of the stellar bar being either a long thin bar with half length of 4 kpc and a position angle of $\phi_{LB} \simeq 45^o$ with respect to the Sun - Galactic Center line, or a triaxial bulge with length 2.5 kpc and a position angle of $\phi_{TB} \simeq 20^o$ or both of them superposed and finds that the latter is the more plausible result.

Historically the spiral arms have been characterized using optical data of young O and B stars, radio observations of the 21 cm line of neutral hydrogen, giant HII regions and CO emission [Oort, Kerr & Westerhout 1958; Simonson 1970; Georgelin & Georgelin 1976]. From the maps of OB associations and HII regions, the CO emissions and the massers in high-mass star-forming regions a four-armed pattern arise from the data [Georgelin & Georgelin 1976, Taylor & Cordes 1993, Vallée 2008, Reid et al. 2009], whereas from the COBE K-band observations (i.e. using the FIR and NIR emission) (Drimmel & Spergel 2001) and the IR Spitzer/GLIMPSE survey (Churchwell et al. 2009) only two major arms appear. These major arms are traced by stellar population (young and mainly old) as enhancements in the spiral tangencies. Though it may not be a general property of galaxies (Eskridge et al. 2002), many galaxies classified as flocculent or multi-armed systems in blue, display a two-armed grand design in the K-band [Block et al. 1994; Kendall, Kennicutt & Charke 2011].

The pattern speed of a non-axisymmetric feature, such as the Galactic bar or the spiral structure, is defined as the rotational velocity a non-inertial reference frame should be rotating at so the structure is at rest. This velocity is a principal dynamical parameter, as it determines the orbital structure of the stars in the disk. The difficulty on studying the large-scale structure and the dynamics of our own Galaxy due to our position within it is the reason of the large uncertainty associated with the determination of the pattern speed of the Galactic bar and of the spiral arms.

Previous attempts to determine the pattern speed of the Galactic bar have used different methods. The first method consists on comparing the gas flow in hydrodynamic simulations with the observed Galactic CO and HI lv-diagrams (Englmaier & Gerhard 1999), whereas the second method estimates the pattern speed from the assumption that the Galactic bar is rotating fast (as observed in external galaxies) and the length of the bar (for the COBE/DIRBE bar see Binney et al. 1997 and Bissantz & Gerhard 2002; for the long bar see Benjamin et al. 2005 and Cabrera-Lavers et al. 2007). The third method is based on the interpretation of stellar streams observed in the stellar velocity distribution in the solar neighbourhood as due to resonant families near the outer Lindblad resonance (OLR) of the Galactic bar (Dehnen 2000).

The assumption of a constant pattern speed for the spiral arms throughout the disk ($\Omega_{sp} = \Omega_{sp}(\rho)$ where ρ is the galactocentric radius) is not clear a priori, but it is a good first approximation. The most direct method to determine the pattern speed of the spiral arms consists on determining the birthplaces of observed open clusters. If the assumption that open clusters are born in the spiral arms is correct, the distribution of birthplaces for some age bin should be spiral-like, and by comparing the spiral distribution for different age bins, the rotation rate can be estimated (Dias and Lépine 2005). Some other methods used are the computation of the gas flow in realistic Galactic potentials and the comparison with the observed CO lv-diagrams (Bissantz et al. 2003) and the study of the self-consistent response of the Galactic disk to the two-armed K-band spiral pattern proposed by Drimmel & Spergel (2001) as a function of its pattern speed (Martos et al. 2004).

A good determination of the pattern speeds of the Galactic bar and the spiral arms is important to constrain the current galaxy formation models, as it gives clues on the formation of these structures. In an scenario in which the two non-axisymmetric features were formed at the same time, as could be inferred from the observation that many spirals connect with the bar ends, they would be dynamically coupled and we should observe similar pattern speeds for both of them. But, from the most recent observations, the Galactic bar would rotate rapidly with a pattern speed most likely to be in the range $\Omega_p \simeq 50 - 60\,\mathrm{km\,s^{-1}\,kpc^{-1}}$ (corresponding to a bar with a corrotation radius at $R_{CR} \simeq 3.5 - 4\,\mathrm{kpc}$), whereas the spiral arms would rotate much slower with a pattern speed in the range $\Omega_p \simeq 17 - 28\,\mathrm{km\,s^{-1}\,kpc^{-1}}$ (see Gerhard 2011). These results would indicate that the Galactic bar and the spiral structure in the Milky Way are dynamically decoupled.

The Tremaine - Weinberg method (TW hereafter), described in Tremaine and Weinberg (1984), was first derived to determine the pattern speed of external barred galaxies. The importance of this method relies in its simplicity, as it only depends on kinematic arguments to determine the pattern speed. Another major advantage of this method in front of others is its independence of the model. Only three assumptions were made to derive the method: the disk of the galaxy has zero thickness (i.e. any position in the disk can be described with the cartesian coordinates in the disk, (x, y)), the disk has a well-defined pattern speed Ω_p and the surface brightness of the tracer obeys the continuity equation.

Given that our position as observers within the Milky Way Galaxy (MWG hereafter) disk gives a unique viewing geometry which does not permit the TW method to be used, Debattista et al. (2002) derive an equivalent method that mantains the best characteristics of the TW; its simplicity and its model independency. As with the original TW method, the surface density of the tracer has to be constant at a reference frame rotating at a

given pattern speed Ω_p and it has to satisfy the continuity equation. Moreover, the tracer has to be dynamically relaxed so it has felt the perturbation of the non-axisymmetric feature. Given that one of the assumptions of both the TW method and the method derived by Debattista et al. (2002) is that the disk has a well defined pattern speed, Debattista et al. (2002) argue that, in the case our galaxy had several non-axisymmetric structures with different pattern speeds each (as it seems to be in reality), the method would be able to determine an average of these angular velocities, but not each of them separately. This consideration is important as it influences the choice of the tracer for each feature.

The determination of the pattern speed of the Galactic bar done by Debattista et al. (2002) is considered the most direct method to determine it (Gerhard 2011). The authors use a sample of ~ 250 OH/IR stars in the inner galaxy and apply their derivation of the TW method, obtaining a value for the difference between the pattern rotation velocity and the circular velocity of the Local Standard of Rest (LSR). The exact values for the pattern speed depend on the Galactic constants $R_\odot$ and $V_{\rm LSR}$ and the radial velocity of the LSR, $u_{\rm LSR}$. Assuming the LSR follows a circular orbit ($u_{\rm LSR} = 0\,{\rm km\ s^{-1}}$) and using the values $R_\odot = 8.5\,{\rm kpc}$ and $V_{\rm LSR} = 220\,{\rm km\ s^{-1}}$ (Allén & Santillán 1991), they obtain a pattern speed for the bar of $\Omega_{p,b} = 59 \pm 5 \pm 10\,{\rm km\ s^{-1}\ kpc^{-1}}$, where the last uncertainty is systematic and due to the population used not being fully relaxed.

Upcoming all-sky surveys, such as Gaia or APOGEE-I/II, will provide information on the three-dimensional positions and velocities with unprecedented accuracy of the biggest volume of the galaxy ever seen (e.g. Gaia will observe 1 billion stars around the Sun). All that data will help unveil some of the unknowns of our Galaxy. As the surveys will reach farther distances and given the small observational errors, the data obtained from these surveys may be used to determine dynamical parameters such as the pattern speed of the non-axisymmetric structures contained in the Milky Way.

Our main goal is to study and characterize the derivation of the TW method done by Debattista et al. (2002) to study whether it would be applicable to be applied over Gaia data to determine the pattern speed of the Galactic bar and the spiral arms of the MWG. To do so, we start applying it over very simplistic simulations, both test particle and N-body, to see how it behaves, then using each time more realistic test particles models until we end up using Gaia mock catalogues.

2. Methodology

2.1. The Tremaine - Weinberg method

The second assumption of the Tremaine - Weinberg method, *The disk has a well-defined pattern speed* Ω_p, states that the surface density μ of a certain tracer has to satisfy:

$$\mu(x, y, t) = \mu(\rho, \Psi - \Omega_p t) \tag{1}$$

where (x,y) are the cartesian coordinates on the plane of the disk and (ρ, Ψ) are the corresponding polar coordinates. This condition can be understood as a constant surface density at a reference frame rotating at angular speed Ω_p.

Using the continuity equation and ensuring the visible surface density satisfies eq. 1, Tremaine and Weinberg (1984) show that the pattern speed of an external galaxy can be determined from:

$$\Omega_p \sin(i) = \frac{\int_{-\infty}^{\infty} h(Y) \int_{-\infty}^{\infty} V_{\rm los}(X,Y)\mu(X,Y)dXdY}{\int_{-\infty}^{\infty} h(Y) \int_{-\infty}^{\infty} X\mu(X,Y)dXdY} \tag{2}$$

where i is the inclination of the galaxy with respect to the line-of-sight, $\mu(X, Y)$ is the visible surface density of the tracer, $V_{\rm los}$ is the velocity along the line-of-sight, $h(Y)$ is an arbitrary continuous weight function introduced by the authors and (X, Y) are galaxy-centered coordinates along the major and minor axis of the disk, respectively. This method requires a tracer of the non–axisymmetric feature that satisfies the continuity equation. For each structure the ideal tracer may change, but in general, the best tracers for this method are the old populations, as they are spread all over the disk and their kinematics have been influenced by the perturbation of the non-axisymmetric potential introduced by the structure. The conversion between atomic and molecular states precludes gas to be used as a tracer, though some modelling can be used to describe such conversions (Bienaymé et al. 1985).

2.2. The Tremaine - Weinberg method for the Milky Way

In Kuijken & Tremaine (1991) it is shown that the continuity equation can be used to derive an expression for the MWG. Debattista et al.(2002) starts from their two dimensional derivation and expands it to three dimensions for an inertial frame. After discussing the different terms that appear in the equation, they reformulate it to take into account the solar motion, given that any measured radial velocities would be heliocentric. The expression found by Debattista et al. (2002) to determine the pattern speed in a three dimensional non-inertial frame is:

$$\begin{aligned} \Omega_p R_\odot - V_{\rm LSR} &= \frac{\sum_i f(r_i)\left(v'_{r,i} + \mathbf{v}_\odot \cdot \hat{r}_i\right)}{\sum_i f(r_i)\sin(l_i)\cos(b_i)} - \\ &- \Pi_{LSR} \frac{\sum_i f(r_i)\cos(l_i)\cos(b_i)}{\sum_i f(r_i)\sin(l_i)\cos(b_i)} \\ &\equiv \frac{\mathcal{K}}{\mathcal{P}} - \Pi_{LSR}\frac{\mathcal{S}}{\mathcal{P}} \end{aligned} \tag{3}$$

where $R_\odot$ is the galactocentric radius of the Sun, $\Pi_{\rm LSR}$ and $V_{\rm LSR}$ are the radial and tangential velocities of the Local Standard of Rest (LSR hereafter), respectively, $f(r)$ is an arbitrary analytical function described as selection function (i.e. the probability of detecting the tracer), $v'_{r,i}$ is the heliocentric radial velocity, $\mathbf{v}_\odot \cdot \hat{r}_i$ is the projection of the peculiar motion of the Sun in the radial direction and (l, b) are the galactic longitude and latitude, respectively.

For our study we have assumed a circular orbit for the LSR ($\Pi_{\rm LSR} = 0$) and the equation can be rewritten as:

$$\Omega_p = \frac{1}{R_\odot}\left(\frac{\sum_i f(r_i)\left(v'_{r,i} + \mathbf{v}_\odot \cdot \hat{r}_i\right)}{\sum_i f(r_i)\sin(l_i)\cos(b_i)} + V_{\rm LSR}\right) = \frac{1}{R_\odot}\left(\frac{\mathcal{K}}{\mathcal{P}} + V_{\rm LSR}\right) \tag{4}$$

where the pattern speed Ω_p is determined from a ratio between two quantities, $\mathcal{K}$ and $\mathcal{P}$, which are further described in eq. 5.

Looking into the expressions, the numerator $\mathcal{K}$ is summing the contribution of the radial velocities over all the particles, thus measuring the asymmetry in the kinematics field (i.e. when summing over all the galactic longitudes, the radial velocities of the

particles following the axisymmetric potential will have opposite signs and they will cancel out). In the case of the denominator $\mathcal{P}$, it is summing over the y position of the particles as if all of them had heliocentric radius of unity (in our models the Sun is located over the x-axis). This quantity represents the asymmetry in the density distribution of the particles, as the contribution of the particles whose position has not been perturbed by the non-axisymmetric potential will cancel out. From eq. 5 we can see that these quantities can be understood as the sum of the contributions of the positive galactic longitude region and the negative region, or of the inner region (1st and 4th quadrants) and the outer region (2nd and 3rd quadrants). This idea will allow a more detailed study of the contribution to the determination of the pattern speed of each region of the galaxy.

$$\mathcal{K}_{\pm} = \sum_{i\,|\,l_i \gtrless 0^{\rm o}} f(r_i)\left(v'_{r,i} + \mathbf{v}_{\odot}\cdot\hat{r}_i\right) \quad \rightarrow \quad \mathcal{K} = \mathcal{K}_{+} + \mathcal{K}_{-}$$
$$\mathcal{P}_{\pm} = \sum_{i\,|\,l_i \gtrless 0^{\rm o}} f(r_i)\sin(l_i)\cos(b_i) \quad \rightarrow \quad \mathcal{P} = \mathcal{P}_{+} + \mathcal{P}_{-} \tag{5}$$

In his derivation, Debattista et al. (2002) assume that any perturbation to the axisymmetric potential is due to the presence of a non-axisymmetric feature. They argue that if that structure can be contained within a certain range in galactic longitude, the summatories can be restricted to the particles contained in that region, as the rest of the disk will only feel the axisymmetric potential and both their radial velocities and their positions will cancel out. But it has been observed in several studies (Antoja et al. 2009, 2011 and Monari 2014) that, given a non-axisymmetric structure such as the Galactic bar or some spiral arms, even if the overdensity due to the feature could be contained within a certain range of galactic longitude, the kinematic perturbation is being felt all over the galactic disk forming the so called moving groups, which are overdensities in the velocity distribution. Given this result, we are interested in studying whether the assumption done by Debattista et al. (2002) can be applied over our models.

2.3. Characteristics of the method

As discussed in eq. 3, Debattista et al. (2002) introduce an analytic function $f(r)$ as part of his derivation and defines it as the detection probability of the discrete tracers. We study the method considering two possibilities for the selection function $f(r)$. In the first case, we consider that all particles have the same probability of being detected, thus, $f_1 = 1$, whereas in the second case we consider as detected all particles within a certain limiting radius r_{lim} for $l \in [0, 360^{\rm o}]$ (i.e. a radial step function):

$$f_3(r) = \begin{cases} 1 & r \leq r_{lim} \\ 0 & r > r_{lim} \end{cases} \tag{6}$$

Our intention when using this selection function is to try to reproduce the observational constraints due to the interstellar extinction and the limitation in the detected flux with the distance.

2.4. Strategy for the estimation of the error on Ω_p

In order to determine the statistical errors, we study the accuracy of the TW method based on three aspects: the size of the sample (i.e. the number of particles N considered), the sampling used given a certain size N and the effect of the initial random generation of particles.

First, we compute the TW method for different number of particles given a certain model and selection function. With this study we intend to determine the minimum/maximum number of particles to obtain a good determination of the pattern speed. Then, we compute the TW method for the same number of particles as for the previous exercise, but doing several computations at each size (between $2 - 10$, depending on how many subsampling of that size could be done in the original sample), so we can do an initial estimation of the error bars as half the dispersion observed. Finally, we study what would have happened to the recovered pattern speed if the sample would have been slightly different due to a different initial random initialization. To do so, we use the bootstrap statistical method of random sampling with replacement, which consists of reordering the particles in the original sample allowing the repetition and the replacement of some of them, obtaining a slightly different sample with which the pattern speed is recomputed. We have repeated this process 1000 times to have a good distribution of the pattern speed to be able to use its 75% confidence interval (CI hereafter) as error bars.

2.5. Study of the asymmetry

As described in eq. 4, the TW method determines the pattern speed from a ratio between the asymmetry in the kinematics (represented by $\mathcal{K}$) and the asymmetry in the density (represented by $\mathcal{P}$). Given that these quantities can be determined from the contribution of the inner/outer regions of the galaxy or the positive/negative regions in galactic longitude, their study may shed some light on the structure of the galaxy.

In the case of an axisymmetric model, it is obvious that its asymmetries will be null, and thus, the method does not hold for it and the pattern speed will diverge.

Another interesting question is how do the physical characteristics of the models used influence the asymmetry detected. Debattista et al. (2002) define two parameters that quantify and normalize each asymmetry so different models can be compared between them:

$$A_{\mathcal{K}} = \frac{|\mathcal{K}|}{|\mathcal{K}_{+}| + |\mathcal{K}_{-}|}; \quad A_{\mathcal{P}} = \frac{|\mathcal{P}|}{|\mathcal{P}_{+}| + |\mathcal{P}_{-}|} \tag{7}$$

where $A_{\mathcal{K}/\mathcal{P}} = 1$ describes a completely asymmetric model. We use these parameters to study such influence.

3. Simulations and disk mock catalogues

In order to properly test the method, we use different types of simulations, varying either the physical characteristics of the method or the type of simulation. We can classify them by the way the simulations were generated: test particle, N-body simulations or mock catalogues.

A summary of their characteristics can be found in Table 1. The columns, from left to right, contain the type of simulation, the name of the model, the imposed pattern speed $\Omega_{p,sim}$, the initial radial velocity dispersion σ_U, the amplitude of the spiral arms A_{sp}, the non-axisymmetric feature contained in the model and the size of the simulation.

It is important to note the differences between our simulations and the ones used by Debattista et al. (2002). The authors used very simplistic simulations describing either a central bar or spiral arms and showed that they were capable of recovering $\Delta V \equiv \Omega_p R_{\odot} - V_{\rm LSR}$ with average errors of $\sim 17\%$ for samples of 500 stars. In our study we use more realistic simulations and

we work with samples of minimum $N = 10^6$ particles. The increase in the number of particles is due to the low asymmetries in our models, that require a larger sample to obtain the same asymmetry signal.

3.1. Simulations with analytical potential

A test particle simulation corresponds to a simulation in which an analytic galactic potential is set at the beginning and the particles are evolved within it. If the system is evolved for a sufficiently large time, at the end it becomes dynamically relaxed. The advantage of this type of simulation to test the TW method is that, given that one imposes the pattern speed of the non-axisymmetric feature as part of the initial conditions, we can use it to verify how accurately the method is recovering it.

Depending on the type of potential set at the beginning, different structures may arise. In this study we use an axisymmetric simulation and the simulations with a Galactic bar described in Romero-Gómez et al. (2015) and the simulations of spiral arms described in Antoja et al. (2011).

The total galactic potential used for the three types of simulations consists of an axisymmetric component and, in the case of the two latter types of simulations, a non-axisymmetric potential that describes either the Galactic bar or the spiral arms. The three types of simulations use the Allen & Santillán (1991) potential for the axisymmetric component. This potential consists of the superposition of a bulge, a flattened disk and a massive spherical halo. The first two are described as Miyamoto-Nagai potentials (Miyamoto & Nagai 1975), and the halo is built as a spherical potential.

The Galactic bar is described as a 3D bar with a boxy bulge plus a long bar using a superposition of two Ferrers ellipsoids (Ferrers 1877) with non-homogeneity index equal to $n = 1$ (Romero-Gómez et al. 2011, Martínez-Valpuesta & Gerhard 2011). We study three different bar simulations, in which the only difference between them is the imposed pattern speed Ω_p (ranging from 40 to 60 km s^{-1} kpc^{-1}). It is important to note that the mass of bulge has transferred to the bar at the end of the integration, so the total mass is conserved. On the other hand, the spiral arms are described using the TWA model. This model was derived by Lin & Shu under the Tight-Winding Approximation; instead of deriving the dispersion relation for a general spiral wave, they assumed a small pitch angle in order to neglect distant perturbations (Binney & Tremaine 2008; Lin et al. 1969). In this case, we study five different simulations which they had either different pattern speed Ω_p, or radial velocity dispersion σ_U, or amplitude of the spiral arms A_{sp}, to see the effects of each physical parameter on the method.

3.2. N-body simulations

An N-body simulation is a simulation that has been solved self-consistently, that is, solving Poisson's and Boltzsmann equation at each time step. These are more complex simulations than the test particle, as the final potential is given from the final distribution of particles and it cannot be known beforehand.

We use the models NBB1 and NBB5 from Roca-Fàbrega et al. (2013, 2014). These are fully self-consistent models with a live exponential disk and live dark matter Navarro Frenk White (NFW) halo, run with the pure N-body adaptive refinement tree (ART) code (Kratsov et al. 1997).

The main difference between these models and the test particle models is that the resulting pattern speed is not constant through the disk ($\Omega_p \neq \Omega_p(\rho)$), though it can be used as a first approximation that it is, thus being a more complex situation (but also more realistic) for the TW method to correctly recover the pattern speed.

3.3. Mock catalogues

A mock catalogue is a representation of what a detector is going to observe assuming a certain tracer. In our case, we are interested in reproducing observations done by the Gaia satellite and we choose two different tracers for the disk: Red Clump (RC hereafter) K-giants (K0-1 III stars) and F0 stars. In the case of the K-giants we assume they have an absolute magnitude of $M_K = -1.61$ (Alves 2000) without intrinsic dispersion in brightness and intrinsic colors of $(V-I)_o = 1.0$ and $(V-K)_o = 2.34$ (Alves 2000), whereas for the F0 type stars we use an absolute magnitude of $M_V = 2.95$ (Wainscoat et al. 1992) and an intrinsic color of $(V-I)_o = 0.36$ (Ducatti 2001).

The reason for choosing these tracers is that they represent populations that are neither too young nor too old. If one considers a tracer representing an old population, its velocity dispersion will be really large (old populations are also known as hot populations) and the perturbation in the density will be too small to detect, whereas if one considers a tracer representing a young population, its kinematics will not have been influenced by the galactic potential yet and they will still correspond to the kinematics of the birthplace. For that, the ideal populations to use as tracers are those that are middle aged. Moreover, the tracers chosen have a high intrinsic brightness, allowing them to be detected from farther away, and thus, to cover a larger volume of the galaxy.

In order to produce the mock catalogues, we first assign the corresponding physical parameters of each tracer to the simulation that more closely represents its kinematics. In the case of the F0 type stars, we assign them to the model TWA0 as it corresponds to a simulation with a low velocity dispersion, typical of a young population (Antoja et al. 2016), whereas for the RC giants we have assigned them to the models barR22 (Romero-Gómez et al. 2015) and TWA10, representing a central bar and spiral arms respectively, as they have larger values of velocity dispersion corresponding to an older population.

For the mock catalogues of spiral arms, we then apply the Drimmel extinction (Drimmel et al. 2003) over the models chosen to obtain the absorption each particle of the simulation suffers due to the interstellar dust. We use the code presented in Romero-Gómez et al. (2015), updated to post-launch perfomance as described in de Bruijne et al. (2014) to simulate the Gaia errors, restricting our sample to those stars with $G_{rvs} \leq 16.1$, the limiting magnitude for the spectrometer on board of Gaia. In this way we obtained the two mock catalogues TWA0_F and TWA10_RC. This process reduces the size of our simulations from 2×10^7 particles to $\sim 7.5 \times 10^5$ particles in the case of F stars and $\sim 3.3 \times 10^6$ particles in the case of the RC giants. This difference is due the higher intrinsic brightness of the RC giants in front of the F stars, that make them easier to detect from farther away.

In an attempt of controlling the effect of the observational errors in the determination of the pattern speed, we restrict the mock catalogues for spiral arms to those stars with $\sigma_\pi/\pi < 10\%$ and $\sigma_{RV} < 10$ km s^{-1}, producing the mock catalogues TWA0_F_sbsm and TWA10_RC_sbsm. This constraint reduces the size of the sample by a third.

In the case of the mock catalogue for the bar model, we are interested in studying separately the effect of the interstellar ex-

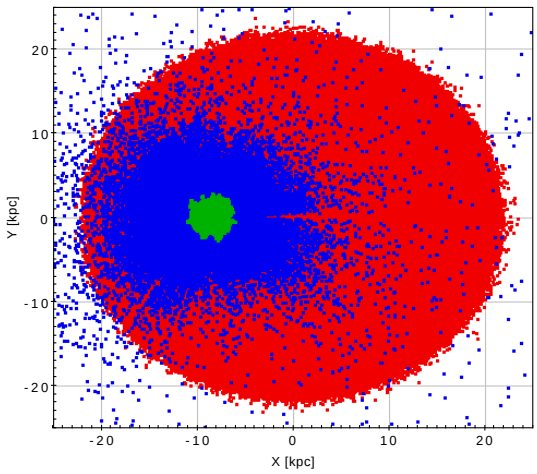

Fig. 1. Representation of the positions (X, Y) for the model TWA0 (red dots) and the mock catalogues TWA0_F (blue dots) and TWA0_F_sbsm (green dots) in which we assume F0 stars to be the tracers. The first mock catalogue contains all F stars expected to be seen by Gaia with $G_{RVS} \leq 16.1$, whereas in the second mock catalogue the observational errors are constrained to be $\sigma_\pi/\pi < 10\%$ and $\sigma_{RV} \leq 10\,\mathrm{km\,s^{-1}}$. The Sun is located at the position $(X, Y)|_\odot = (-8.5, 0)$ kpc.

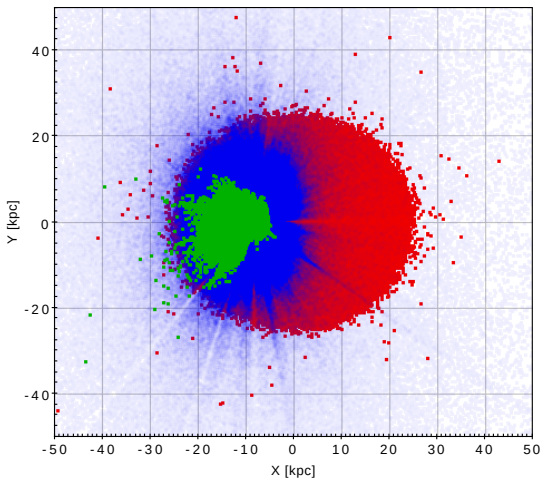

Fig. 2. Representation of the positions (X, Y) for the model TWA10 (red dots) and the mock catalogues TWA10_RC (blue dots) and TWA10_RC_sbsm (green dots) in which we assume RC giants to be the tracers. The first mock catalogue contains all RC giants observed by Gaia with $G_{RVS} \leq 16.1$, whereas in the second mock catalogue the observational errors are constrained to be $\sigma_\pi/\pi < 10\%$ and $\sigma_{RV} \leq 10\,\mathrm{km\,s^{-1}}$. The Sun is located at the position $(X, Y)|_\odot = (-8.5, 0)$ kpc.

tinction and the effect of the observational errors. As described in Romero-Gómez et al. (2015), the original model barR22 reproduces the local surface density of RC stars and it contains $N = 57 \times 10^6$ particles. Over this model we also apply the Drimmel extinction and, aditionally, we apply a cut in the magnitude, $G \leq 20$, that represents the effect of the dust absorption. This constraint produces a sample of $\sim 26.3 \times 10^6$ which we call barR22_G20. Over this sample we apply the Gaia errors as we did for the mock catalogues of spiral arms, restraining to a magnitude $G_{rvs} \leq 15$ and applying a constraint for the observational errors of $\sigma_{RV} < 10\,\mathrm{km\,s^{-1}}$ and $\sigma_\pi/\pi < 10\%$, producing two mock catalogues of $\sim 4.4 \times 10^6$ particles: barR22_RCB and barR22_NOE. The first contains the observational values whereas the second one contains their corresponding real values. Our intention when working with these two mock catalogues is to see whether the determination of the pattern speed is more influenced by the introduction of the observational errors or by the reduction of the sample due to the constraint on the observational errors.

To see more clearly how the extinction and the constraint of the errors affect the distribution of the sample, we plot in Figs. 2 - 3 the positions (X, Y) of the original models and the mock catalogues produced: TWA0, TWA10 and barR22, respectively. In the three figures it can be clearly seen that the interstellar extinction blocks part of the galaxy in the direction of the Galactic Center and introduces an important error in the determination of the heliocentric distance. It is also worth noticing how the constraint in the observational errors reduces the size of the mock catalogue. In the Fig. 4 we plot the distribution of the heliocentric distances for the bar model barR22 and its mock catalogues. It can be seen that the extinction and the constraint in the observational errors limit the maximum distance that can be observed, though the larger values correspond to the direction of the Galactic Anti-Center (as seen in Fig. 3).

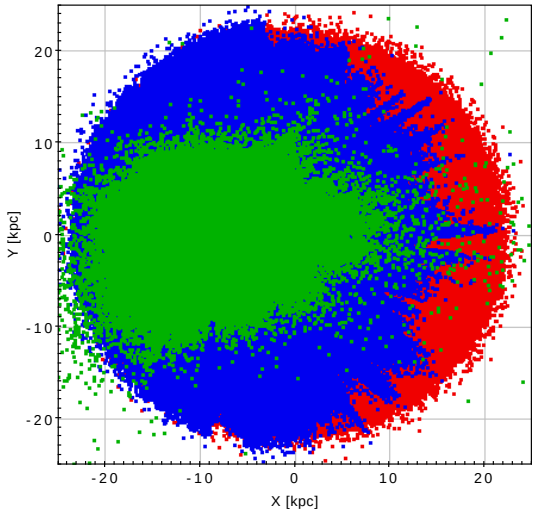

Fig. 3. Representation of the positions (X, Y) for the model barR22 (red dots) and the mock catalogues barR22_G20 (blue dots) and barR22_RCB (green dots) in which we assume RC giants to be the tracers. The first mock catalogue contains the effect of the interstellar extinction on the RC population of the model barR22 ($G \leq 20$), whereas in the second mock catalogue the observational errors are constrained to be $\sigma_\pi/\pi < 10\%$ and $\sigma_{RV} \leq 10\,\mathrm{km\,s^{-1}}$ (i.e. $G_{rvs} \leq 15$). The Sun is located at the position $(X, Y)|_\odot = (-8.5, 0)$ kpc.

3.4. Setting up the initial conditions

For the values of the tangential velocity of the LSR we have used $V_{\mathrm{LSR}} = 220\,\mathrm{km\,s^{-1}}$ for the test particle simulations (Allen & Santillán 1991), $V_{\mathrm{LSR}} = 184\,\mathrm{km\,s^{-1}}$ for the model NBB1 and $V_{\mathrm{LSR}} = 174\,\mathrm{km\,s^{-1}}$ for the model NBB5. N-body simulations require different values due to its scaling. In the case of the Sun's galactocentric radius we have used $R_\odot = 8.5$ kpc (Allen & Santillán 1991) and for its peculiar velocity we have used $\mathbf{v}_\odot = (U, V, W)_\odot = (10.0, 5.25, 7.17)\,\mathrm{km\,s^{-1}}$ (Dehnen & Binney 1998) for the test particle bar models and $\mathbf{v}_\odot = (9, 12, 7)\,\mathrm{km\,s^{-1}}$ for the test particle spiral arms models and the N-body simulations (initial value adopted in Antoja et al. 2011 and Roca-Fàbrega et al. 2013,2014).

Table 1. Summary of the simulations characteristics. The columns, from left to right, contain the type of simulation, the name of the model, the imposed pattern speed $\Omega_{p,sim}$, the initial velocity dispersion σ_U, the amplitude of the spiral arms, the non-axisymmetric feature contained in the model and the size of the simulation.

Type of simulation	Model	Ω_p (km s^{-1} kpc^{-1})	σ_U (km s^{-1})	A_{sp} ((km s^{-1})^2 kpc^{-1})	Non-axisymmetric feature	Number of particles
Test particle	Axisymmetric	0	20	—	None	2×10^7
	barR20	50	30	—	Galactic bar	6×10^6
	barR21	60	30	—		
	barR22	40	30	—		$6 \times 10^6, 57 \times 10^6$
	TWA0	12	20	850	Spiral arms	2×10^7
	TWA1	18	20	850		
	TWA3	30	20	850		
	TWA10	18	40	850		
	TWA12	18	20	1300		
N-body	NBB1	$\sim 30 - 40$	—	—	Bar and spiral arms	$\sim 1 \times 10^6$
	NBB5	$\sim 20 - 25$	—	—		$\sim 5 \times 10^6$
Mock catalogue	TWA0_F	12	20	850	Spiral arms	$\sim 7.5 \times 10^5$ ($\sim 2 \times 10^5$)
	TWA10_RC	18	40	850		$\sim 3.3 \times 10^6$ ($\sim 1 \times 10^6$)
	barR22_G20	50	30	—	Galactic bar	$\sim 26.3 \times 10^6$
	barR22_RCB	50	30	—		$\sim 4.4 \times 10^6$

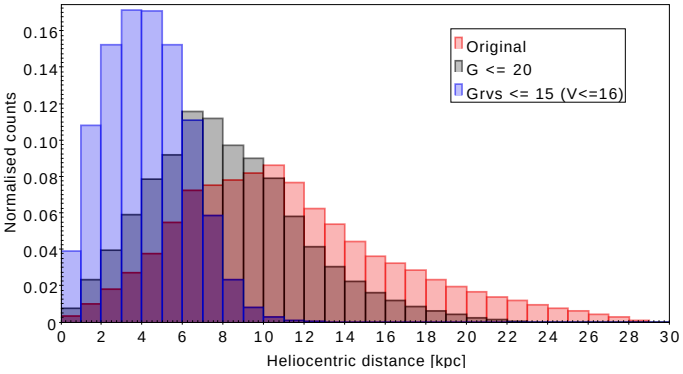

Fig. 4. Distribution of the heliocentric distances for the bar model barR22 (red bars) and the mock catalogues barR22_G20 (grey bars) and barR22_RCB (blue bars) in which we assume RC giants to be the tracers.

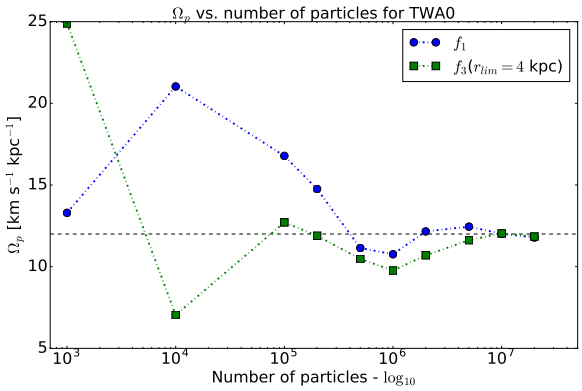

Fig. 5. Recovered pattern speed using the Tremaine - Weinberg method and the selection functions f_1 and $f_3(r_{lim} = 4\,\mathrm{kpc})$ for the spiral arms simulation TWA0 for different sample sizes N. The dashed line corresponds to the imposed pattern speed.

3.5. Practical application

For this thesis we use different programming languages to write the codes (Python 2.7, Python 3.5 and Fortran 77) as well as different technical facilities to run them (personal laptop, computer grid at the Leiden Observatory and Cartesius, SurfSara's supercomputer). There is a summary of some typical computational operations and their approximate wall-clock times in Table 2.

4. Results

4.1. Study of the statistical errors

First, we study the behaviour of the method when applied over samples of different number of particles. In Fig. 5 we plot the recovered pattern speed using the selection functions f_1 and $f_3(r_{lim} = 4\,\mathrm{kpc})$ for the spiral arm model TWA0 and for different number of particles N. It can be seen that the recovered value $\Omega_{p,TW}$ converges towards the imposed $\Omega_{p,sim}$ for large samples using the two selection functions. This result allows us to determine a minimum number of particles, N_{min}, so the method starts converging towards the imposed value. This number depends on the model and on the selection function used, but we consider it to be $N_{min} \simeq 1 \times 10^6$ particles. This behaviour agrees with our expectations, as a small sample does not properly describe the system, and thus, can not be representative of it to obtain a good determination of the pattern speed.

We then study the behaviour of the method when, for a given sample size, we change the sampling used. In Fig. 6 we represent the recovered pattern speed $\Omega_{p,TW}$ for a given size of the sample N using different sampling for the spiral arm model TWA0 and the selection function f_1. We see that the dispersion in the values gets reduced for larger samples, which is in agreement with the previous result. This result allows us to do a first estimation of the error bars as half the size of the dispersion, and so, we can choose a minimum sample size for which the dispersion due to the different sampling is already small enough.

Finally, we study how would the recovered pattern speed change if the sample would have been slightly different. To do so we use the bootstrap statistical method of random sampling with replacement. Fig. 7 (*top*) corresponds to the distribution of pattern speed result of a 1000 bootstrap for the spiral arm simulation TWA0 with $N = 1 \times 10^7$ particles and considering all the particles (selection function f_1). As expected, the recovered pattern speed from the original sample lies within the 75% con-

Table 2. Approximate wall-clock time for some typical computational operations.

What	Simulation	N	Selection function	Time	Computer
TW computation	TWA	1×10^7	f_1 and $f_3(r_{lim} = 3, 4, 5, 6)$ kpc	$\sim$ 10 min	Personal laptop
TW for different N	TWA	1×10^7	f_1	$\sim$ 20 min	Personal laptop
1000 bootstraps	TWA	1×10^7	f_1	$\sim$ 4 h	Cartesius

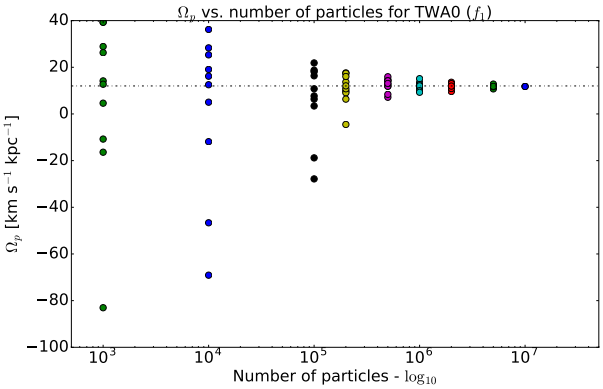

Fig. 6. Recovered pattern speed using the Tremaine - Weinberg method for different samplings given a certain sample size for the spiral arm simulation TWA0 using the selection function f_1. The dashed line corresponds to the imposed pattern speed.

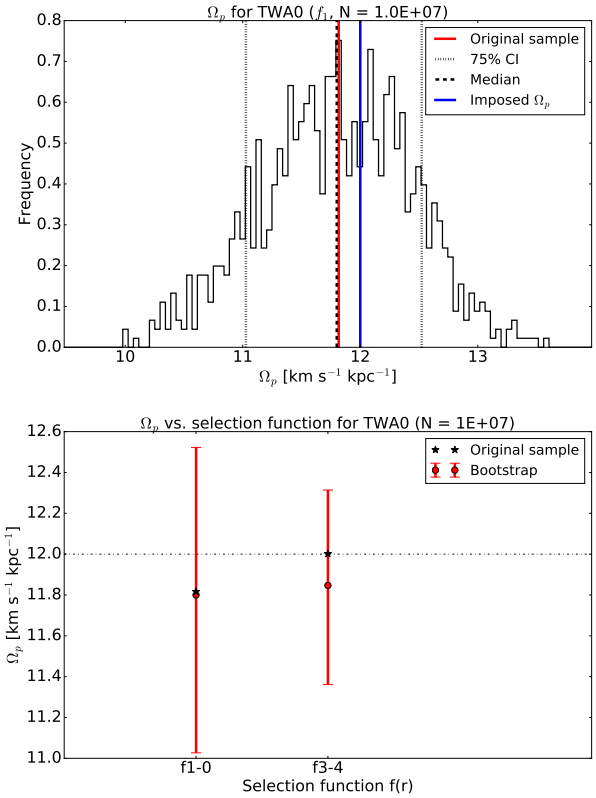

Fig. 7. Result of running 1000 bootsrap of the TW method for the spiral arms simulation TWA0 for N = 1×10^7 particles (*top*) Distribution of $\Omega_{p,TW}$ for the selection function f_1. The dashed black line is the median, whereas the dotted black lines represent the 75% CI. The $\Omega_{p,TW}$ for the original sample is represented by the solid red line and the imposed $\Omega_{p,sim}$ is represented by the solid blue line. (*bottom*) Recovered pattern speed (black stars), median and error bars of each bootstrap distribution (red lines) for the selection functions f_1 and $f_3(r_{lim} = 4\,\mathrm{kpc})$. The dashed line corresponds to the imposed pattern speed.

fidence interval and it agrees with the median of the distribution. Given that the imposed pattern speed is also between the confidence interval, we are properly recovering the pattern speed for this model. Using the 75% confidence interval of the Ω_p distributions as error bars, we have a determination of the statistical error of the method. In Fig. 7 (*bottom*) we represent the pattern speed of the original sample and its correspondent medians and errorbars from the bootstrap for two different selection functions (f_1 and $f_3(r_{lim} = 4\,\mathrm{kpc})$). We can see that for both selection functions the imposed pattern speed lies within the error bars.

4.2. Tremaine - Weinberg method for different models

After studying the reliability of the method on the sample, we want to explore whether the underlying physics of each model may affect the determination of the pattern speed.

To do so, we first examine if the constraint in the galactic longitudes suggested by Debattista et al. (2002) is valid for our models and then we study four different characteristics of the simulations: the pattern speed of the model $\Omega_{p,sim}$, the radial velocity dispersion σ_U, the amplitude of the spiral arms A_{sp} and the type of simulation.

4.2.1. TW method for different galactic longitude ranges

It is interesting to see whether the assumption done by Debattista et al. (2002) of reducing the summatories over a range in the galactic longitude ($|l| \leq l_0$) if the non-axisymmetric feature (and its kinematic perturbations) can be contained in them, is applicable in our models. In Fig. 8 and 9 we represent the results of applying the TW method over the simulations barR20 and TWA0, respectively, for two different cases: the first one considering the particles over $|l| \leq 180^o$ (black round dots) and the second one considering only the particles within $|l| \leq 90^o$ (orange triangles). The pattern speed of the model is represented by the dashed line.

In the case of the Galactic bar, Fig.8 (*top*), we only recover the imposed pattern speed when considering all the particles (f_1) or when going up to, at least, $r_{lim} \simeq 6\,\mathrm{kpc}$. This indicates that the particles contained in the internal region of the model for heliocentric distances less than 6 kpc are not perturbed enough by the bar and the response spiral arms. The better result obtained when going up to $r_{lim} = 6\,\mathrm{kpc}$ is caused by the presence of particles from the bar overdensity, which is starting to be seen.

For the spiral arms, Fig.8 (*bottom*), we can see that the recovered pattern speed in the constrained sample are within $\sim 2 - 3\,\mathrm{km\ s^{-1}\ kpc^{-1}}$ of the pattern speed of the model, except when going up to $r_{lim} = 3\,\mathrm{kpc}$. This result indicates that the internal region in the spiral arms models contains much more information than the external region ($l > 90^o$ and $l < -90^o$).

From the two non-axisymmetric features considered (Galactic bar and spiral arms), only the overdensity of the bar can be contained within a range of galactic longitude and, if the kine-

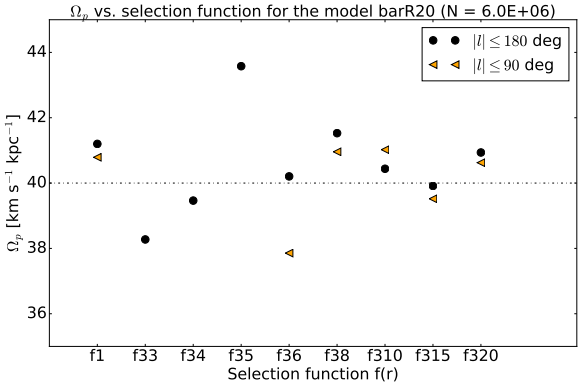

Fig. 8. Result of applying the TW method using different selection functions (f_1 and $f_3(r_{lim} = 3, 4, 5, 6, 8, 10, 15, 20\,\mathrm{kpc})$) over the bar model barR20 using 6×10^6 particles and summing over all the galactic longitudes (black round dots) or over the range $|l| \leq 90^o$ (orange triangles). The dashed line corresponds to the pattern speed of the model.The three outliers correspond to $\Omega_{p,TW} \simeq -60, 0, 20\,\mathrm{km\ s^{-1}\ kpc^{-1}}$, respectively.

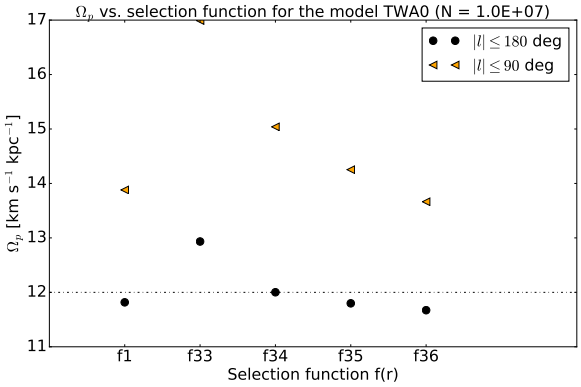

Fig. 9. Result of applying the TW method using different selection functions (f_1 and $f_3(r_{lim} = 3, 4, 5, 6\,\mathrm{kpc})$) over the spiral arms model TWA0 using 1×10^7 particles and summing over all the galactic longitudes (black round dots) or over the range $|l| \leq 90^o$ (orange triangles). The dashed line corresponds to the pattern speed of the model.

matic perturbation can also be contained, the assumption done by Debattista et al. (2002) is correct. Hence, the pattern speed of the Galactic bar can be determined from the inner region of the Galaxy. But in the case of the spiral arms, nor the overdensities nor the kinematic effects can be contained, thus the assumption not being valid for these models (despite the good results obtained). From now on, we decide to use the summatories over all the galactic longitudes when computing the TW method.

4.2.2. TW method and the pattern speed $\Omega_{p,sim}$

We are interested in studying whether the actual value of the imposed pattern speed influences in the accuracy of the TW method. To study this, we use two sets of three different simulations that are identical except for their pattern speeds and that contain a different non-axisymmetric feature. For the Galactic bar we use the test particle simulations barR20, barR21 and barR22, whereas for the spiral arms we use the models TWA0, TWA1 and TWA3.

We start analyzing the results for the bar models. In Fig. 10 (*top*) we represent the absolute error between the imposed pattern speed $\Omega_{p,sim}$ and the recovered pattern speed $\Omega_{p,TW}$ using the selection function f_3 going up to $r_{lim} \in [3, 7]\,\mathrm{kpc}$ with steps of $\sim 0.1\,\mathrm{kpc}$ as a function of the limiting radius r_{lim} for the three bar models. Three divergences, each corresponding to a different model, are clearly visible. The position of these divergences appears to be related to the pattern speed; the model with the lowest angular rotational velocity, barR20, diverges at $\sim 5.2\,\mathrm{kpc}$ whereas the model with the highest angular rotational velocity, barR21, diverges at $\sim 6.1\,\mathrm{kpc}$. This strange behaviour is related to the behaviour of the asymmetry in the density $\mathcal{P}$, which is represented for the three bar models in Fig. 10 (*middle*) using the selection function f_3 as a function of the limiting radius r_{lim}. It can be seen that at the limiting radius at which the divergences occurs, $r_{lim} \simeq 5.2, 5.6, 6.1\,\mathrm{kpc}$, respectively, the corresponding asymmetry in the density is null, $\mathcal{P} \to 0$. This null value is caused by the compensation of the overdensities contained within that limiting radius. This physical reason can be understood with Fig. 10 (*bottom*), which represents the non-axisymmetric structures that have arised in the bar model barR22 at the end of the evolution time. The white cercle has a radius of $r \simeq 5.6\,\mathrm{kpc}$. It can be seen that the Galactic bar is not the only non-axisymmetric feature, as some arms and rings also appear as a response to the bar potential. When one considers a sample up to certain heliocentric radius containing a small portion of the bar, this overdensity coming from the bar is capable of compensating the overdensities due to the other structures, giving a null asymmetry in the densities for that particular radius ($\mathcal{P}|_{r_{lim}} = 0$). As the structures produced during the integration (arms and rings) depend on the pattern speed of the model (i.e. getting stronger with increasing pattern speed), the radius at which the density cancels gets a bit larger with increasing pattern speed (as observed in Fig. 10 (*top*)).

In Fig. 11 (*top*) we represent the equivalent to Fig. 10 (*top*) for the three spiral arms models TWA0, TWA1 and TWA3. The only difference is that the limiting radius studied is $r_{lim} \in [2.5, 6]$ kpc with steps of ~ 0.1 kpc. In this case, we observe that the only model in which the response substructure produces divergences is TWA1, whereas for the other two models, the absolute error is always smaller than $1\,\mathrm{km\ s^{-1}\ kpc^{-1}}$. As previously done for the Galactic bar, in Fig. 11 (*bottom*) we represent the asymmetry in the densities for the three spiral arms models. It can be seen that only the asymmetry corresponding to the model TWA1 crosses $\mathcal{P} = 0$ twice, thus producing the two divergences observed in the top panel of the same figure, as opposite to the other two models, which do not cross the null value. This result indicates that, not only the response structures in the case of the spiral arms depend on the pattern speed of the model, but that the TW method is highly sensitive to them.

4.2.3. TW method and the radial velocity dispersion σ_U

The next physical characteristic we are interested in studying is the radial velocity dispersion. We compare two spiral arms simulations that were generated using two different radial velocity dispersions: TWA1 and TWA10. It has been observed that spiral arms simulations with a higher velocity dispersion are less responsive to the perturbations in the kinematics and in the density (Antoja 2010), so, given that the TW method determines the pattern speed from a ratio between the asymmetry in these two quantities, it is interesting to study whether the value of σ_U affects the determination of the pattern speed. In Fig. 12 (*top*) we find the result of applying the TW method using different selection functions (f_1 and $f_3(r_{lim} = 3, 4, 5, 6\,\mathrm{kpc})$) on a sample of $N = 1 \times 10^7$ particles of TWA1 and TWA10. We can see that the values recovered for both models agree with the imposed pattern

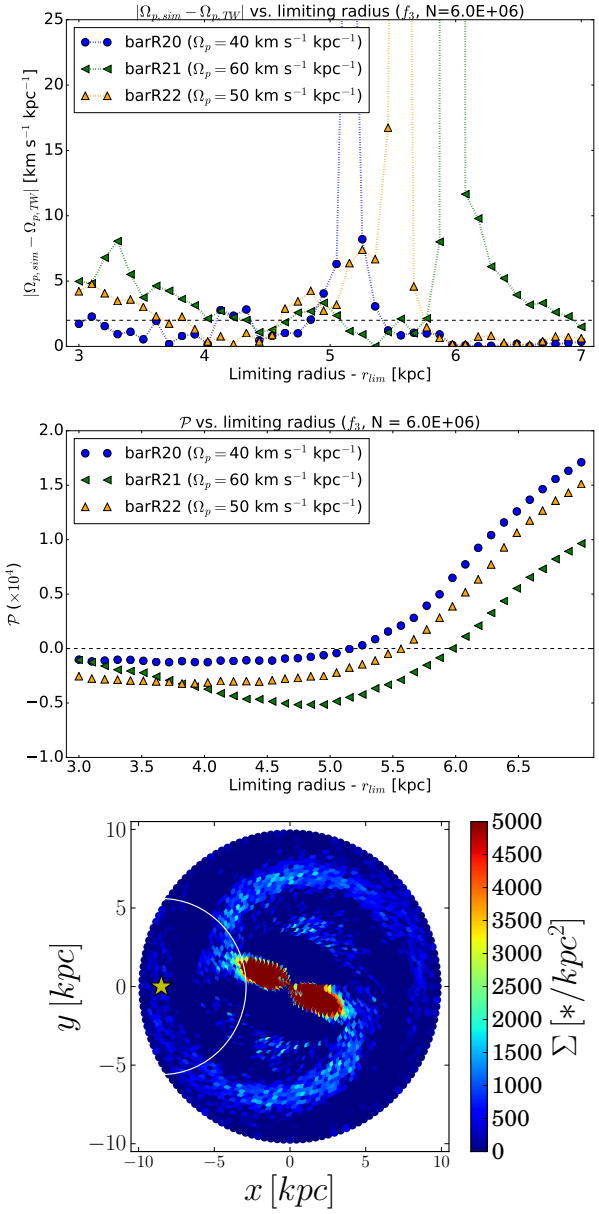

Fig. 10. TW method for Galactic bar simulations with different $\Omega_{p,sim}$. (*top*) Absolute error between the imposed pattern speed ($\Omega_{p,sim}$) and the recovered pattern speed ($\Omega_{p,TW}$) using the selection function f_3 up to $r_{lim} \in [3, 7]$ kpc for the three bar models barR20 (blue dots), barR21 (green triangles) and barR22 (yellow triangles). The dashed line corresponds to an absolute error of 2 km s^{-1} kpc^{-1}; (*middle*) Asymmetry in the density $\mathcal{P}$ for a sample of $N = 6 \times 10^6$ particles of the three bar models using the selection function $f_3(r_{lim} \in [3, 7]$ kpc). The dashed line corresponds to a null asymmetry.; (*bottom*) Surface density (Number of stars /kpc^2) in each of the regions of the non-axisymmetric structures of the bar model barR22. The yellow star shows the Sun position and the white circle has a radius of ~ 5.6 kpc [Romero-Gómez et al. 2015].

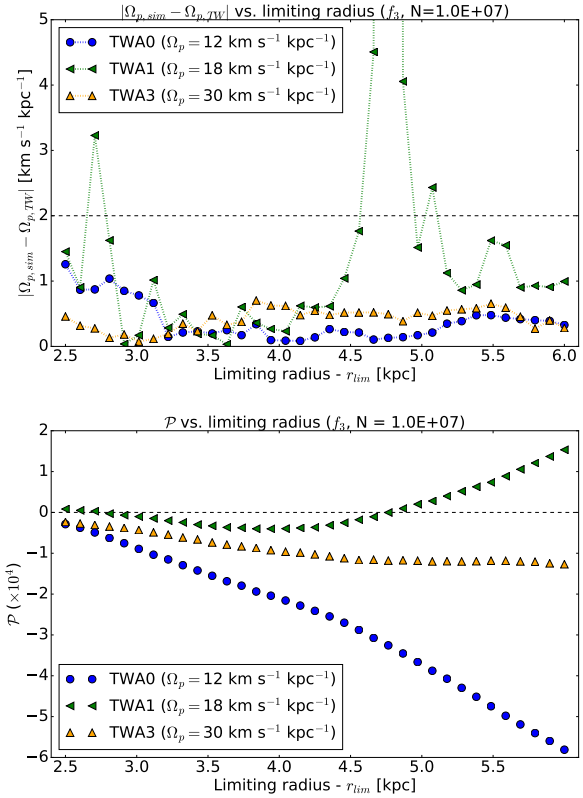

Fig. 11. TW method for spiral arms simulations with different $\Omega_{p,sim}$. (*top*) Absolute error between the imposed pattern speed ($\Omega_{p,sim}$) and the recovered pattern speed ($\Omega_{p,TW}$) using the selection function f_3 up to $r_{lim} \in [2.5, 6]$ kpc for three spiral arms models (TWA0, TWA1 and TWA3). The dashed line corresponds to an absolute error of 2 km s^{-1} kpc^{-1}.(*bottom*) Asymmetry in the density for the three spiral arms simulations using the selection function f_3 as a function of the limiting radius. The dashed line corresponds to a null asymmetry.

speed (represented by the dashed line) when considering both all the sample (f_1) and all particles up to a certain limiting radius (f_3), except when going up to $r_{lim} = 5$ kpc. The small difference between the two models, of ~ 1 km s^{-1} kpc^{-1}, indicates that the velocity dispersion of the population used as tracer does not affect in the determination of the pattern speed. To understand the dispersion observed in $f_3(r_{lim} = 5$ kpc), we represent in Fig. 12 (*bottom*) the absolute error between the imposed pattern speed and the recovered one, $|\Omega_{p,sim} - \Omega_{p,TW}|$, on the same models and for the same number of particles, but only using the selection function f_3 with $r_{lim} \in [2.5, 6]$ kpc with steps of ~ 0.1 kpc. In this figure it can be seen that for both models there is a divergence at $r_{lim} \sim 4.7 - 5$ kpc. This strange behaviour corresponds to the divergences explained earlier, which are caused by a compensation of the overdensities within the model. We have repeated the computation doubling the size of the sample ($N = 2 \times 10^7$ particles) to see if this effect depends on the number of particles considered and we see that it does not depend, as the divergence is still clearly visible.

4.2.4. TW method and the amplitude of the spiral arms A_{sp}

To study the influence of the spiral arms A_{sp} in the determination of the pattern speed, we compare the results for two simulations that are identical except for such amplitude: TWA1 and TWA12. In Fig. 13 (*top*) there is the result of applying the TW method using different selection functions (f_1 and $f_3(r_{lim} = 3, 4, 5, 6$ kpc)) for a sample of $N = 1 \times 10^7$ particles for the models TWA1 and TWA12. It can be seen that when all particles in the sample are being considered (f_1) there is a discrepancy of ~ 2 km s^{-1} kpc^{-1} for both models. But if we consider the particles up to a certain radius r_{lim}, this discrepancy gets smaller, except for the TWA12 model up to $r_{lim} = 3$ kpc. It is particularly interesting that the difference between both models is of ~ 1 km s^{-1} kpc^{-1}, as this

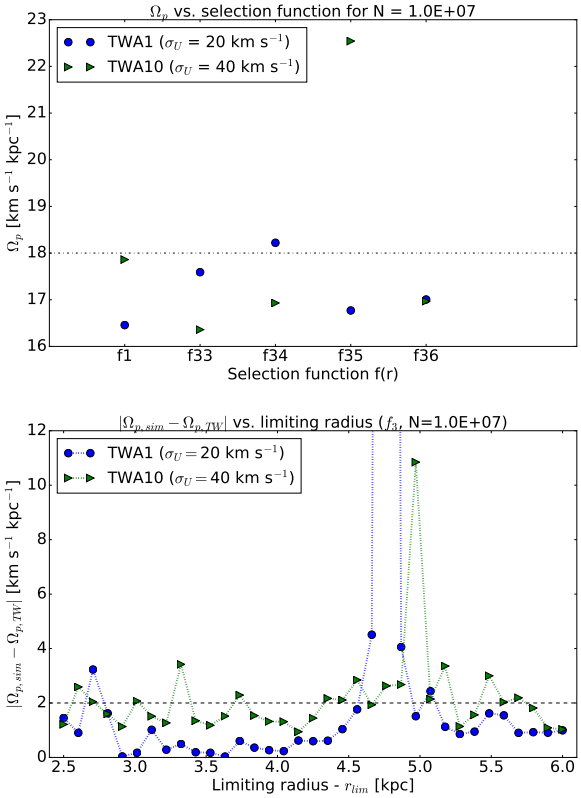

Fig. 12. TW method applied over the spiral arms simulations TWA1 and TWA10. (*top*) Recovered pattern speed $\Omega_{p,TW}$ using different selection functions (f_1 and $f_3(r_{lim} = 3, 4, 5, 6\,\mathrm{kpc})$) on a sample of $N = 1{\times}10^7$ particles for the models TWA1 and TWA10. The dashed line corresponds to the imposed pattern speed; (*bottom*) Absolute error between the imposed pattern speed ($\Omega_{p,sim}$) and the recovered pattern speed ($\Omega_{p,TW}$) using the selection function f_3 up to $r_{lim} \in [2.5, 6]$ kpc. The dashed line corresponds to an absolute error of 2 km s^{-1} kpc^{-1}.

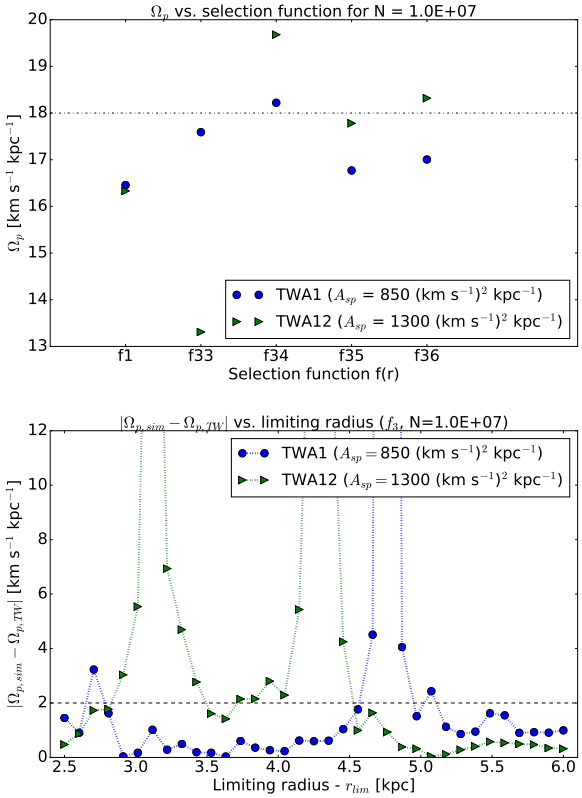

Fig. 13. TW method applied over the spiral arms simulations TWA1 and TWA12. (*top*) Recovered pattern speed $\Omega_{p,TW}$ using different selection functions (f_1 and $f_3(r_{lim} = 3, 4, 5, 6\,\mathrm{kpc})$) on a sample of $N = 1{\times}10^7$ particles for the models TWA1 and TWA12. The dashed line corresponds to the imposed pattern speed; (*bottom*) Absolute error between the imposed pattern speed ($\Omega_{p,sim}$) and the recovered pattern speed ($\Omega_{p,TW}$) using the selection function f_3 up to $r_{lim} \in [2.5, 6]$ kpc. The dashed line corresponds to an absolute error of 2 km s^{-1} kpc^{-1}.

would indicate that the amplitude of the spiral arms does not affect the determination of the pattern speed. In Fig. 13 (*bottom*) we have studied in more detail both simulations using the selection function f_3 for $r_{lim} \in [2.5, 6]$ kpc with steps of ~ 0.1 kpc. It can be seen that the discrepancy found for the model TWA12 model when going up to $r_{lim} = 3$ kpc is due to a divergence in the recovered pattern speed at $r_{lim} \sim 3.1$ kpc. There are two more divergences that do not affect the result in Fig. 13 (*top*), at ~ 4.2 kpc for the model TWA12 and at ~ 4.8 kpc for the model TWA1. As previously discussed, these divergences are due to the fact that the asymmetry in the density is null at that particular r_{lim} in which the overdensities are compensated.

4.2.5. TW method and the different type of simulations

The main reason to test the strength of the TW method on N-body simulations is that these represent a much more realistic case, and thus, a much more complex scenario than the test particle simulations. In the N-body simulations, as compared to the test particle, the outcome of the distribution of particles is not known beforehand, so it may develop more than just one non-axisymmetric structure. In the case of the models we have worked with (NBB1 and NBB5), they contain both a central bar and some spiral arms. The final pattern speed of these structures can be considered constant with the galactocentric radius as a first approximation.

Our intention is to compare the results of applying the TW method to a test particle simulation (TWA0) and to a N-body simulation (NBB5), in order to see whether the more realism and complexity of the N-body simulations affects the accuracy of the method.

In Fig. 14 we plot the absolute error between the pattern speed of the model and the recovered pattern speed, $|\Omega_{p,sim} - \Omega_{p,TW}|$, for the models TWA0 and NBB5 for different selection functions (f_1 and $f_3(r_{lim} = 3, 4, 5, 6\,\mathrm{kpc})$) for different sample sizes, the dashed line corresponding to an absolute error of 2 km s^{-1} kpc^{-1}. It is important to note the outlier for the model NBB5 when using the selection function in which all particles have the same weight (f_1), the value is at $|\Omega_{p,sim} - \Omega_{p,TW}| \simeq 104$ km s^{-1} kpc^{-1}. When considering all particles we may be introducing some extra information (i.e. some kinematic perturbations not caused by the non-axisymmetric feature) that erases the weak trace of the pattern speed, thus recovering a very biased value. Except for that, the rest of the recovered pattern speed agree relatively well with the pattern speed of the model.

4.3. Study of the asymmetry

From eq. 5, one can understand the asymmetries in the kinematics and in the density as the sum of the contributions between the regions with positive/negative galactic longitude. But they can also be understood as the sum of the contributions between

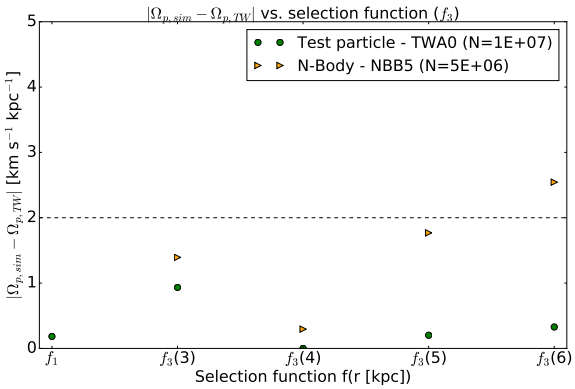

Fig. 14. Absolute error between the imposed pattern speed $\Omega_{p,sim}$ and the recovered pattern speed $\Omega_{p,TW}$ for the models TWA0 and NBB5 as a function of the selection functions $f(r)$ (f_1 and $f_3(r_{lim} = 3, 4, 5, 6\,\mathrm{kpc})$). Note there is an outlier for the model NBB5 at the selection function f_1, the value is at $|\Omega_{p,sim} - \Omega_{p,TW}| \simeq 104\,\mathrm{km\,s^{-1}\,kpc^{-1}}$. The dashed line corresponds to an absolute error of $2\,\mathrm{km\,s^{-1}\,kpc^{-1}}$.

the inner region of the galaxy (1st and 4th quadrants) and the outer region (2nd and 3rd). With these idea, in Fig. 15 we represent the contribution of the inner region (green dots) and the contribution of the outer region (yellow dots) to the asymmetry in the kinematics (*top*) and in the density (*bottom*). We also include the total asymmetries computed from the sum over the positive/negative regions in galactic longitude (black dots) and over the inner/outer regions of the disk (red dotted line). As expected, these two quantities agree. This study allows us to determine that, even though most of the contribution to the asymmetries come from the inner part of the galaxy, the outer part has also some contribution to the determination of the pattern speed and cannot be neglected.

We have seen that the asymmetries in the kinematics and in the density play an important role in the determination of the pattern speed. It would be interesting to study such asymmetries and to compare them between different types of models. To do so, we use the normalized quantifiers defined in eq. 7, where $A_{\mathcal{K}/\mathcal{P}} = 1$ indicate maximum asymmetry, and we study three cases, the first two including only spiral arms and the third being a comparison between the different types of simulations.

The first case we study corresponds to two identical spiral arms simulations except for their radial velocity dispersion σ_U: TWA1 and TWA10. The result of plotting the asymmetry parameters computed at each bootstrap when using the selection function f_1 can be found in Fig. 16. As expected, the simulation corresponding to a cold tracer (TWA1, low velocity dispersion) has higher values of the asymmetry both in the kinematics and in the density when compared to a simulation that corresponds to a hot tracer (TWA10, high velocity dispersion).

For our second case we study if the amplitude of the spiral arms A_{sp} influenced the asymmetry of the models, and to do so, we compared two spiral arms simulations identical except for the amplitude of the arms: TWA1 and TWA12. The result of plotting the asymmetry parameters computed at each bootstrap when using the selection function f_1 can be found in Fig. 17. We can see that for a higher amplitude, i.e. higher intensity of the force done by the spiral arms, it corresponds a higher asymmetry both for the kinematics and for the density, which is in agreement to what it was expected as the amplitude of the perturbed surface density is proportional to the amplitude of the spiral perturbing potential through Poisson's equation (Contopoulos & Grosbøl 1986).

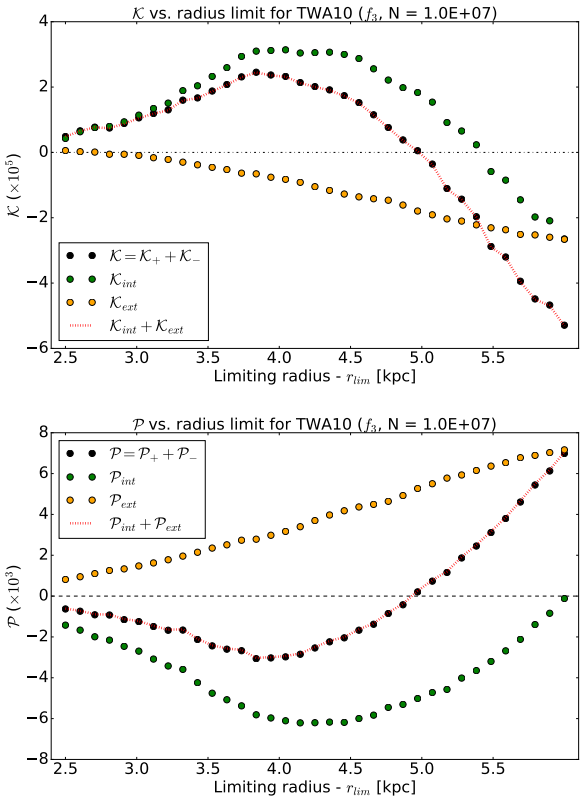

Fig. 15. Asymmetry in the (a) kinematics and in the (b) density as a function of the limiting radius when using the selection function f_3 for the model TWA10 and a sample size of $N = 1 \times 10^7$ particles. We represent the contribution of the inner region (green dots) and of the outer region (yellow dots), as well as the total asymmetries computed from the sum over the positive/negative regions in galactic longitude (black dots) and over the inner/outer regions of the disk (red dotted line).

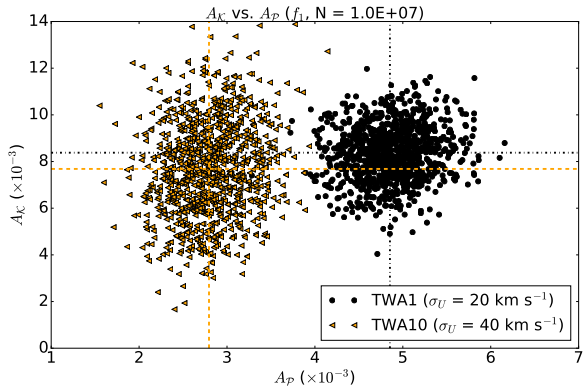

Fig. 16. Representation of the asymmetry parameter for the kinematics ($A_{\mathcal{K}}$) versus the asymmetry parameter for the density ($A_{\mathcal{P}}$) for the spiral arms simulations TWA1 (black dots) and TWA10 (orange triangles). The value of the asymmetry parameters come from a 1000 bootstrap performed using the selection function f_1 and all the sample ($N = 1 \times 10^7$ particles).

For the third case we compare the normalized asymmetries for a test particle Galactic bar simulation (barR22), a test particle spiral arms simulation (TWA0) and a N-body simulation (NBB5). We are interested in studying how does the type of non-axysimmetric feature influence in the asymmetry of the model.

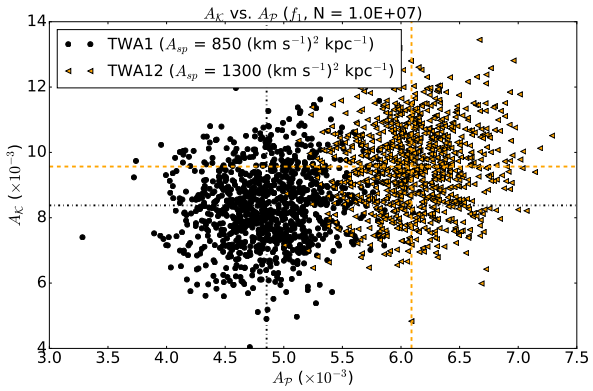

Fig. 17. Representation of the asymmetry parameter for the kinematics ($A_\mathcal{K}$) versus the asymmetry parameter for the density ($A_\mathcal{P}$) for the spiral arms simulations TWA1 (black dots) and TWA12 (orange triangles). The value of the asymmetry parameters come from a 1000 bootstrap performed using the selection function f_1 and all the sample ($N = 1 \times 10^7$ particles).

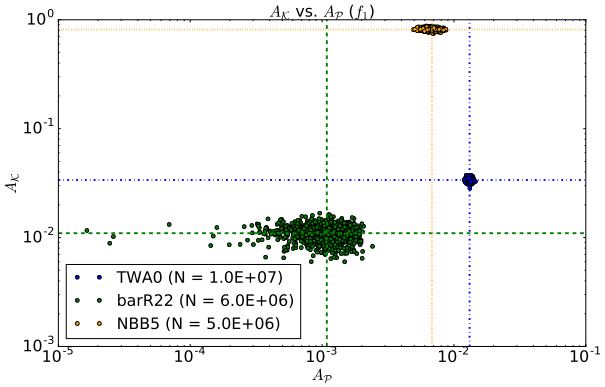

Fig. 18. Representation of the asymmetry parameter for the kinematics ($A_\mathcal{K}$) versus the asymmetry parameter for the density ($A_\mathcal{P}$) for the models TWA0 (blue dots), barR22 (green dots) and NBB5 (orange dots). The value of the asymmetry parameters come from a 1000 bootstrap performed using the selection function f_1 and all the sample.

In Fig. 18 we represent the asymmetry parameters computed during the bootstrap using the selection function f_1 for the three models described. We can observe that the N-body simulation has the largest asymmetries in the kinematics, but the spiral arms simulation have the largest asymmetries in the density. Moreover, we can observe that the Galactic bar introduces smaller perturbations (almost one order of magnitude less), both in the kinematics and in the density, than the spiral arms. This is due to the bar being low-massive, $M = 10^{10}$ M$_\odot$, whereas the Milky Way bar is being considered nowadays to be $M \simeq 2{-}3{\times}10^{10}$ M$_\odot$ (Wang et al. 2012, Wegg et al. 2015).

5. Particular cases: axisymmetric model and tracers

5.1. Axisymmetric model

We use an axisymmetric model to study whether the method is capable of recovering the correct pattern speed even with the absence of a non-axisymmetric structure. We try both selection functions (f_1 and f_3) with different r_{lim} in the case of f_3, but for all of them the results are far from the imposed null pattern speed. Given that the method determines the pattern speed from a ratio between the asymmetry in the kinematics and the asymmetry in the density, the lack of asymmetry in the density distribution for the axisymmetric model makes $\mathcal{P} \to 0$, and thus, the ratio diverges and the imposed value can not be recovered, as it was expected.

5.2. Tracers

We apply the Tremaine - Weinberg method over all the mock catalogues described in Section 3.3 using the selection function f_1. We choose to only apply this function as we consider that the selection of the particles as a function of the extinction and the magnitude has already been considered with the absorption and the cuts in magnitude.

A summary of the values obtained can be found in Table 3. The columns describe, from left to right, the non-axisymmetric structure contained in the model, the tracer used, the pattern speed of the model $\Omega_{p,sim}$, the model or mock catalogue used, the errors applied, the recovered pattern speed $\Omega_{p,TW}$, the 75% CI and the number of particles used for the computation.

In the case of the mock catalogues for the spiral arms models, we only recover the imposed pattern speed when using the mock catalogue TWA10_RC in which we have only the extinction and the Gaia errors. For all the other cases, the recovered pattern speed is not in agreement with the imposed one. There are two possible explanations for that. The first one is that the observational errors in the distance and in the radial velocity modify the sample so much that the small perturbations in the kinematics and in the density that the TW method uses to trace back the pattern speed are erased and, thus, lead to a wrong determination. And the second possible reason may be the size of the mock catalogue, as we have seen in Section 4.1 that a minimum number of particles is required to properly described the system and so, to be able to recover the right pattern speed.

In order to see whether the mock catalogues for spiral arms are representative of what Gaia is going to observe, we use the GUMS model, which is a simulated catalogue of the sources expected to be seen by Gaia. Robin et al. (2012) describe this model, whose Galactic sources are based on the Besançon Galactic Model and includes Galactic thin and thick disks, bulge and halo, based on appropriate density laws, kinematics, star formation histories, enrichment laws, initial mass function, and total luminosities for each of the populations.

For the F stars and doing a cut for $G_{rvs} < 17$, the GUMS model is left with $\sim 8.9 \times 10^7$ stars. This result is two orders of magnitude larger than our largest mock catalogue for F stars. The low intrinsic brightness of this tracer and the cut in magnitude cause the sample to be very reduced in helicoentric distances, and thus, to not properly represent the non-axisymmetric perturbation. This leads us to conclude that the F stars can not be used as tracers for this method.

In the case of the RC giants and doing a cut for $G_{rvs} < 17$, Gaia is going to observe $\sim 1.26{\times}10^8$ stars, which is two orders of magnitude larger than our largest mock catalogue of RC giants. But in this case we are correctly recovering the pattern speed for the mock catalogue in which we have not imposed a constraint on the observational errors, TWA10_RC. The constraint appears to be limiting the sample too much. This result indicates that the RC giants may be a good possible tracer to apply the TW method.

Given that the bar model barR22 reproduces the surface density of the RC stars in the Solar Neighbourhood, the mock catalogues produced from it have enough particles and are representative of what Gaia is going to observe. From the results in Table

Table 3. Summary of the values obtained for the mock catalogues. The columns describe, from left to right, the non-axisymmetric structure contained in the model, the tracer used, the pattern speed of the model $\Omega_{p,sim}$, the model or mock catalogue used, the errors applied, the recovered pattern speed $\Omega_{p,TW}$, the 75% CI and the number of particles used for the computation.

Non-axisymmetric feature	Tracer	$\Omega_{p,sim}$ (km s^{-1} kpc^{-1})	Model / Mock catalogue	Errors applied	$\Omega_{p,TW}$ (km s^{-1} kpc^{-1})	75% CI		N
Spiral arms	F stars	12	TWA0	Original	11.8	11.0	12.5	1×10^7
			TWA0_F	$G \leq 20 + G_{rvs} \leq 16.1$	52.5	48.3	57.9	7.5×10^5
			TWA0_F_sbsm	Subsample	26.4	26.2	26.6	$\sim 2 \times 10^5$
	RC giants	18	TWA10	Original	17.9	12.6	19.2	1×10^7
			TWA10_RC	$G \leq 20 + G_{rvs} \leq 16.1$	18.5	18.3	18.6	3.5×10^6
			TWA10_RC_sbsm	Subsample	30.3	30	30.6	$\sim 1 \times 10^6$
Galactic bar	RC giants	50	barR22	Original	63.8	50.9	92.3	6×10^6
			barR22_G20	Extinction - $G \leq 20$	26.03	26.01	26.04	$\sim 26.3 \times 10^6$
			barR22_NOE	Ext. + $G_{rvs} \leq 15$ (real)	24.952	24.941	24.953	$\sim 4.4 \times 10^6$
			barR22_RCB	Ext. + $G_{rvs} \leq 15$ (errors)	24.953	24.948	24.960	$\sim 4.4 \times 10^6$

3 we can see that the recovered pattern speed does not agree with the imposed one nor even for the original model. In order to do a more extensive study, we represent in Fig. 19 the absolute error between the imposed pattern speed and the recovered one, $|\Omega_{p,sim} - \Omega_{p,TW}|$, as a function of the limiting radius when using each model for all its particles and the selection function f_3. This selection function is further constraining the smaller samples (i.e. the cut in magnitude applied can also be understood as a cut in distance), but it allows to study whether the introduction of the extinction and the Gaia errors in the mock catalogues has an effect on the structure of the model (i.e. the divergences inform us of the compensation of overdensities). It can be seen that the extinction, represented by the mock catalogue barR22_G20, does not affect much the determination of the pattern speed, as the errors are within ~ 2 km s^{-1} kpc^{-1} for the radius up to $r_{lim} \simeq 5$ kpc. Further away, the determination becomes much worse. In the case of the mock catalogues with the Gaia errors (barR22_NOE represents the real values and barR22_RCB represents the observational values), we can see there is no difference between them at all, but the recovered pattern speed is really far away from the imposed value, $|\Omega_{p,sim} - \Omega_{p,TW}| \sim 25$ km s^{-1} kpc^{-1}. The fact that for both catalogues we obtain such a bad result would indicate that the sample obtained from the constraint over the observational errors is not the best one to describe the system. Romero-Gómez et al. (2015) observe that, after introducing the observational errors for Gaia, the particles did not properly trace the Galactic bar anymore. Hence, it is not the sample but the introduction of the observational errors what mostly affects the determination of the pattern speed.

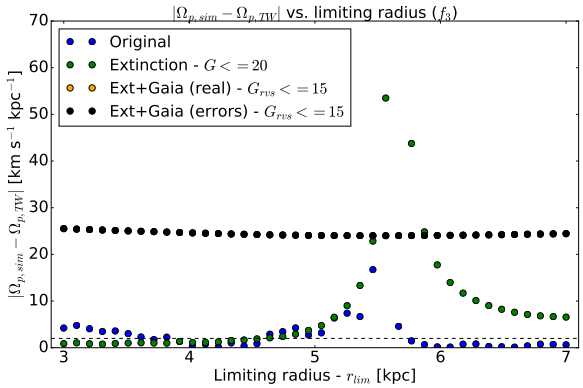

Fig. 19. (*top*) Absolute error between the imposed pattern speed ($\Omega_{p,sim}$) and the recovered pattern speed ($\Omega_{p,TW}$) using the selection function f_3 up to $r_{lim} \in [3, 7]$ kpc for the model barR22 and the mock catalogues barR22_G20 (extinction - $G \leq 20$), barR22_NOE (real values after extinction + Gaia errors with $G_{rvs} \leq 15$) and barR22_RCB (observational values after extinction + Gaia errors with $G_{rvs} \leq 15$). The dashed line corresponds to an absolute error of 2 km s^{-1} kpc^{-1}.

6. Discussion

6.1. Requirements of the method

The study of the method on some simplistic cases has allowed us to see some of its requirements:

(1) The at present development of the TW method assumes a constant pattern speed throughout the disk, $\Omega_p = \Omega_p(\rho)$ where ρ is the galactocentric radius.

(2) As expected, a good knowledge of the selection function highly influences in the result. This function can account for the lack of asymmetry introduced by the interstellar extinction in the form of weighting the particles, but in our study for the galactic tracers we considered all the particles in the mock catalogue with equal weight. We assume the probability of detecting the particles is being applied with the extinction and the cut in distance, and we recover the imposed pattern speed in the case of the RC giants for spiral arms.

(3) The method requires an all-sky sample in order to determine the pattern speed of the spiral arms, but this can be constrained to the inner part of the Galaxy for the Galactic bar if the tracers go up to the bar. The sample of tracers used has to be cover a sufficiently high volume of the galaxy, arriving to $r \simeq 2 - 3$ kpc in the case of the spiral arms and $r \geq 6$ kpc in the case of the Galactic bar. For the tracers used, we see that the F stars do not satisfy this, whereas the RC giants do.

(4) The method is highly sensitive to the stellar density distribution of the tracer population, producing divergences in the recovered pattern speed if the overdensities get compensated when doing a cut in distance. The best strategy to overcome this is,if the sample is big enough, to do a study of the pattern speed going up to different limiting radius to localize the divergences (as they may give information on the extra structures generated by the non-axisymmetric feature) and to identify the imposed pattern speed as the value at which the recovered pattern speed tends to.

6.2. Will the Tremaine - Weinberg method be applicable to real data?

We need all-sky spectroscopic surveys (or complementing surveys) for the spiral arms such as Gaia, APOGEE I and II (north and south, respectively) and WEAVE and 4MOST (north and

south, respectively) and spectroscopic surveys centered in the Galactic center for the Galactic bar.

The good recovery of the pattern speed for the spiral arm mock catalogue of disk RC stars (see Table 3), and the fact that Gaia is expected to observe two orders of magnitude more RC giants than the ones contained in our simulations, indicates that this method is able to determine the pattern speed of the spiral arms near solar galactocentric radius with a good precision. Unfortunately, in the case of the bar mock catalogue, it seems that the Gaia errors introduced erase the imprint of the bar perturbation and the correct pattern speed can not be correctly recovered using only radial velocity data, thus WEAVE and 4MOST will be needed.

As mentioned, the data can also come from complementing surveys such as APOGEE-I and APOGEE-II which look to the north and south hemispheres, respectively. The northern survey has already been completed and the data is available, but the southern survey is still undergoing.

The difference with Gaia is that they do not cover all sky, only discrete samplings over the Galactic Plane and they may not be symmetric between them, so a more complex selection function must be designed and implemented.

Nowadays, all previous attempts of determining the pattern speed of the Galactic bar and the spiral arms show that they are not the same, being $\Omega_{p,b} \simeq 50\,\mathrm{km\,s^{-1}\,kpc^{-1}}$ and $\Omega_{p,sp} \simeq 18-30\,\mathrm{km\,s^{-1}\,kpc^{-1}}$, respectively (Gerhard 2011). Debattista et al. (2002) argue that, if several pattern speeds exist in the disk, the recovered pattern speed will be the average one. Hence, this method is not capable of distinguishing both pattern speeds. In the future, we might overcome this problem by studying different ranges in distance and using distinctive tracers for the Galactic bar and the spiral arms.

A way to improve the method could be if, instead of being derived only for radial velocities, a new mathematical development is done using proper motion data. As known, the Gaia survey will provide a much larger proper motion survey with higher accuracy than the radial velocity survey.

7. Summary and conclusions

The main goal of this thesis is to evaluate whether the TW method as derived by Debattista et al. (2002) will be applicable to determine the pattern speed of the Galactic bar and the spiral arms of the Milky Way. To do so, we use test particle and N-body simulations, as well as test particle mock catalogues using both hot and cold tracers. We examine independently two non-axisymmetric features in the test particle simulations, a Galactic bar and two TWA spiral arms, which correspond to simplistic cases. We characterize the statistical errors as the 75% CI of the bootstrap distribution of recovered pattern speeds.

We can summarize the work done in this thesis when evaluating the application of the TW method considering radial velocity data and knowledge of the heliocentric distance of the stars as follows:

(i) The results from Sect. 4.2.1 indicate that the method needs to be applied to all-sky data in order to determine the pattern speed of the spiral arms, but it can be constrained to the inner region of the Galaxy (as long as the sample arrives up to, at least, $r \simeq 6\,\mathrm{kpc}$) for the determination of the Galactic bar.

(ii) Studying the recovered pattern speed when applying the TW method to different sample sizes and different subsampling given a sample size (see Figs. 5 and 6), we see that, for samples larger than a certain number of particles, the model is better described. We can consider that number to be $N_{min} \simeq 10^6$ particles for both the Galactic bar and the spiral arms.

(iii) Eq. 5 indicate that both the asymmetries in the kinematics and in the density can be studied for different galactic regions (see Fig. 15).

(iv) Since the pattern speed is determined from a ratio of the two asymmetries, a compensation in the overdensities when going up to a certain radius cause the pattern speed to diverge (see Fig. 10 (*top*)), thus making the method very sensitive to the stellar density distribution of the tracer population. The strength of the response structures increase with the imposed pattern speed, so the limiting radius at which the compensation occurs also increases with the pattern speed of the model (see Fig. 10 (*middle*)).

(v) The constant pattern speed assumed by the method and the existence of two non-axisymmetric features instead of one, play an important role in the poor determination of the pattern speed for the N-body simulations (see Fig. 14).

(vi) In the spiral arm case, neither the strength of the arms nor the tracer used influence in the determination of the pattern speed, as the absolute errors are of the order of $\sim 2\,\mathrm{km\,s^{-1}\,kpc^{-1}}$, with respect to the pattern speed of the model (see Figs. 12 and 13).

(vii) As expected and as seen in Figs. 16 and 17, both the cold tracers and the strongest spiral arms introduce larger asymmetries in their respective models when compared to equal models for hot tracers and weak spiral arms, respectively.

(viii) The low mass of the bar introduces smaller asymmetries than the TWA spiral arms and the higher complexity of the N-body simulations is reflected in larger kinematic asymmetries (see Fig. 18).

(ix) The extinction applied on the bar model barR22 does not affect the determination of the pattern speed when doing cuts in distance, but the introduction of the Gaia errors erase the imprints of the bar (as seen in Romero-Gómez et al. 2015) and leads to a wrong determination of the pattern speed (as seen in Fig.19).

The main conclusions of this work are:

1. In order to recover the imposed pattern speed, the sample has to cover all-sky and has to go up to $r \simeq 2-3\,\mathrm{kpc}$ for the spiral arms models, whereas for the Galactic bar, the sample can be constrained to the inner region of the Galaxy if it goes up to $r \geq 6\,\mathrm{kpc}$.
2. The limitation on the heliocentric distance covered due to the low intrinsic brightness of the F stars and the small size of our mock catalogues (two orders of magnitude less than what Gaia is expected to observe), make this tracer not suitable for the TW method.
3. The TW method can be applied to RC giants observed by Gaia to determine the pattern speed of the spiral arms.
4. The symmetry requirement proves to be esencial for the determination of the pattern speed, thus being necessary for the new large spectroscopic surveys such as WEAVE and 4MOST to satisfy it. We hope the teams designing the future large spectroscopic surveys take into account this suggestion.

Acknowledgements. I would like to thank Dr. Figueras, Dr. Romero-Gómez, Dr. Roca-Fàbrega and Dr. Antoja for the time and the patience. This work was supported by the European Space Agency and the Erasmus+ programme for master students.

References

[1] Allen, C., Santillán, A. 1991, Revista Mexicana de Astronomia y Astrofisica, 22, 255
[2] Alves, D.R. 2000, ApJ, 539, 732
[3] Antoja, T., Valenzuela, O., Pichardo, B., Moreno, E., Figueras, F., & Fernández, D. 2009, ApJ, 700, L78
[4] Antoja, T. 2010, PhD Thesis, Universitat de Barcelona
[5] Antoja, T. Figueras, F., Romero-Gómez, M., Pichardo, B., Valenzuela, O., & Moreno, E. 2011, MNRAS, 418, 1423-1440
[6] Antoja, T., Roca-Fàbrega, S., de Bruijne, J., & Prusti, T. 2016, A & A, 589, A13
[7] Benjamin, R. A., et al. 2005, ApJ, 630, L149
[8] Bienaymé O., Bosma A., Athanassoula E. 1985, in Cosmical Gas Dynamics, ed. F. D. Kahn, (Utrecht: VNU Science Press), pg. 205
[9] Binney, J., Gerhard, O., & Spergel, D. 1997, MNRAS, 288, 365
[10] Binney, J., Tremaine, S. 2008, Galactic Dynamics, Second Edition, Princeton Univ. Press, Princeton
[11] Bissantz, N., & Gerhard, O. 2002, MNRAS, 330, 591
[12] Bissantz, N., Englmaier, P., & Gerhard, O. 2003, MNRAS, 340, 949
[13] Blitz, L., & Spergel, D. N. 1991, ApJ, 379, 631
[14] Block D. L., Witt A. N., Grosbøl P., Stockton A., Moneti A., 1994, A&A, 288, 383
[15] de Bruijne, J. H. J., Rygl, K. L. J., Antoja, T. 2014, in EAS PS, 67, 23
[16] Cabrera-Lavers, A., Hammersley, P. L., González-Fernández, C., López-Corredoira, M., Garzón, F., Mahoney, T. J. 2007, A & A, 465, 825-838
[17] Contopoulos G., Grosbøl P., 1986, A&A, 155, 11
[18] Churchwell E. et al., 2009, PASP, 121, 213
[19] Debattista, V. P., Gerhard, O., & Sevenster, M. N. 2002, MNRAS, 334, 355-368
[20] Dehnen, W., Binney, J. 1998, MNRAS,298, 387
[21] Dehnen, W. 2000, AJ, 119, 800
[22] Dias, W. S., & Lépine, J. R. D. 2005, ApJ, 629, 825
[23] Drimmel R., Spergel D. N., 2001, ApJ, 556, 181
[24] Drimmel, R., Cabrera-Lavers, A., López-Corredoira, M., 2003, A & A, 409, 205
[25] Ducati, J.R., Bevilacqua, C.M., Rembold, S.B., Ribeiro, D. 2001, ApJ, 558, 309-322
[26] Dwek, E., Arendt, R. G., Hauser, M. G., et al. 1995, ApJ, 445, 716
[27] Englmaier, P., & Gerhard, O. 1999, MNRAS, 304, 512
[28] Eskridge P. B. et al., 2002, ApJS, 143, 73
[29] Ferrers N. M. 1877, Q.J. Pure Appl. Math., 14, 1
[30] Georgelin Y. M., Georgelin Y. P., 1976, A&A, 49, 57
[31] Gerhard, O. 2011, Memorie della Societa Astronomica Italiana Supplement, 18, 185
[32] Hammersley, P. L., Garzón, F., Mahoney, T., & Calbet, X. 1994, MNRAS, 269, 753
[33] Kendall S., Kennicutt R. C., Clarke C., 2011, MNRAS, 414, 538
[34] Kravtsov, A. V., Klypin, A. A., & Khokhlov, A. M. 1997, ApJS, 111, 73
[35] Kuijken K., Tremaine S. 1991, Dynamics of Disc Galaxies, ed. B. Sundelius (Göteborg: Sweden) pg. 71
[36] Lin C. C., Yuan C., Shu F. H., 1969, ApJ, 155, 721
[37] López-Corredoira, M., Cabrera-Lavers, A., Mahoney, T. J., Hammersley, P. L., Garzón, F., González-Fernández, C. 2007, ApJ, 133, 154-161
[38] Martinez-Valpuesta, I.; Gerhard, O. 2011, ApJ, 734, L20
[39] Martos, M., et al. 2004, MNRAS, 350, L47
[40] Miyamoto, M., Nagai, R. 1975, PASJ, 27, 533
[41] Monari, G. 2014, PhD thesis, University of Groningen
[42] Oort J. H., Kerr F. J., Westerhout G., 1958, MNRAS, 118, 379
[43] Reid M. J. et al., 2009, ApJ, 700, 137
[44] Robin, A. C., Luri, X., Reylé, C., Isasi, Y., Grux, E., Blanco-Cuaresma, S., Arenou, F., Babusiaux, C., Belcheva, M., Drimmel, R., Jordi, C., Krone-Martins, A., Masana, E., Mauduit, J. C., Mignard, F., Mowlavi, N., Rocca-Volmerange, B., Sartoretti, P., Slezak, E., Sozzetti, A. 2012, A & A, 543, A100
[45] Roca-Fàbrega, S., Valenzuela, O., Figueras, F., et al. 2013, MNRAS, 432, 2878
[46] Roca-Fàbrega, S., Antoja, T., Figueras, F., et al. 2014, MNRAS, 440, 1950
[47] Romero-Gómez, M., Athanassoula, E., Antoja, T., Figueras, F. 2011, MNRAS, 418, 1176
[48] Romero-Gómez, M., Figueras, F., Antoja, T., Abedi, H., & Aguilar, L. 2015, MNRAS, 447, 218-233
[49] Simonson S. C., 1970, A&AS, 9, 163
[50] Stanek, K. Z., Mateo, M., Udalski, A., et al. 1994, ApJ, 429, L73
[51] Taylor J. H., Cordes J. M., 1993, ApJ, 411, 674
[52] Tremaine, S. & Weinberg, M. D. 1984, ApJ, 282, L5-L7
[53] Vallée, J.P. 2008, ApJ, 135, 1301
[54] Vallée, J.P. 2015, MNRAS, 450, 4277-4284
[55] Wainscoat, R.J. & Cowie, L.L., 1992, A.J., 103, 332
[56] Wang, Y., Zhao, H., Mao, S., Rich, R. M. 2012, MNRAS, 427, 1429-1440
[57] Weinberg, M. D. 1992, ApJ, 384, 81
[58] Wegg, C., Gerhard, O., Portail, M. 2015, MNRAS, 450, 4050-4069

Appendix A: Results of applying the Tremaine - Weinberg method on the simulations

A summary of the recovered pattern speed, with its 75% CI, for all the models and mock catalogues can be found in Table A.1. The columns contain, from left to right, the type of simulation, the non-axisymmetric feature contained, the model, the imposed pattern speed $\Omega_{p,sim}$, the selection function $f(r)$ used, the recovered pattern speed $\Omega_{p,TW}$, the 75% CI and the number of particles used for the computation.

Table A.1. Summary of the recovered pattern speed with its 75%CI interval for all the models and mock catalogues. From left to right, the columns contain the type of simulation, the non-axisymmetric feature contained, the model, the imposed pattern speed $\Omega_{p,sim}$, the selection function $f(r)$ used, the recovered pattern speed $\Omega_{p,TW}$, the 75% CI and the number of particles used for the computation.

Type of simulation	Non-axisymmetric feature	Model	$\Omega_{p,sim}$ (km s^{-1} kpc^{-1})	$f(r)$	$\Omega_{p,TW}$ (km s^{-1} kpc^{-1})	75% CI		Number of particles
Test particle	Galactic bar	barR20	40	f_1	41,2	37,1	45,9	6×10^6
				$f_3(r_{lim} = 4\,\mathrm{kpc})$	39,5	36,2	45,4	
		barR21	60	f_1	-2067,6	-386,7	399,6	
				$f_3(r_{lim} = 4\,\mathrm{kpc})$	58,0	54,9	61,6	
		barR22	50	f_1	63,8	50,9	92,3	
				$f_3(r_{lim} = 4\,\mathrm{kpc})$	49,0	46,5	52,1	
	Spiral arms	TWA0	12	f_1	11,8	11,0	12,5	10^7
				$f_3(r_{lim} = 4\,\mathrm{kpc})$	12,0	11,4	12,3	
		TWA1	18	f_1	16,5	15,2	18,5	
				$f_3(r_{lim} = 4\,\mathrm{kpc})$	18,2	13,9	18,6	
		TWA3	30	f_1	26,3	23,7	31,4	
				$f_3(r_{lim} = 4\,\mathrm{kpc})$	29,4	29,1	30,0	
		TWA10	18	f_1	17,9	12,7	19,2	
				$f_3(r_{lim} = 4\,\mathrm{kpc})$	16,9	14,4	19,0	
		TWA12	18	f_1	16,3	16,5	19,3	
				$f_3(r_{lim} = 4\,\mathrm{kpc})$	19,7	8,6	20,1	
N – body	Galactic bar and spiral arms	NBB1	35	f_1	-1,9	-2,9	-0,9	$\sim 10^6$
				$f_3(r_{lim} = 4\,\mathrm{kpc})$	30,2	29,7	30,8	
		NBB5	25	f_1	129,7	119,5	142,2	$\sim 5 \times 10^6$
				$f_3(r_{lim} = 4\,\mathrm{kpc})$	24,7	24,5	24,9	
Mock catalogue	Spiral arms	TWA0_F	12	f_1	52,5	48,3	57,9	$\sim 7.5 \times 10^5$
		TWA0_F_sbsm			26,4	26,2	26,6	$\sim 2 \times 10^5$
		TWA10_RC	18		18,5	18,4	18,6	$\sim 3.5 \times 10^6$
		TWA10_RC_sbsm			30,3	29,9	30,6	$\sim 1 \times 10^6$
	Galactic bar	barR22_G20	50		26,03	26,02	26,05	$\sim 2.63 \times 10^7$
		barR22_NOE			24,952	24,941	24,953	$\sim 4.4 \times 10^6$
		barR22_RCB			24,954	24,948	24,959	